Aerodynamic Interaction Effects Between a Propeller Slipstream and Single Slotted Flap

Plijter, J.C.; Duivenvoorden, R.R.; Sinnige, T.

DOI
10.2514/6.2025-0667

Publication date
2025

Document Version
Final published version

Published in
Proceedings of the AIAA SCITECH 2025 Forum

AIAA SciTech Forum
6-10 January 2025, Orlando, FL
AIAA SCITECH 2025 Forum

10.2514/6.2025-0667

Aerodynamic Interaction Effects Between a Propeller Slipstream and Single Slotted Flap

Jurriën C. Plijter*, Ramon R. Duivenvoorden.† and Tomas Sinnige‡
Delft University of Technology, Delft, The Netherlands

A 3D unsteady RANS simulation utilizing the Spalart-Allmaras (SA) turbulence model was conducted to investigate aerodynamic interactions within a propeller-wing-flap system. The research specifically examines the complex flow field around a slotted flap, highlighting the interaction between the propeller slipstream and the main wing and flap during powered high-lift conditions. Operating conditions include a chord-based Reynolds number of 2 million, with thrust and flap settings reflecting take-off conditions ($J = 0.765$, $T_c = 1.267$, $\delta_f = 15°$) at an angle of attack $\alpha = 8.3°$. Chordwise pressure distributions and surface shear stress contours show strong agreement with previous experimental measurements and oil flow visualizations of the same geometry. Findings indicate that a portion of the propeller slipstream transfers from the pressure side of the main wing to the upper side of the flap through the cove, dominating the flap flow field. Although the upper side of the main wing experiences fluctuating flow originating from the propeller slipstream, this flow does not induce unsteadiness or penetrate the flap upper side boundary layer along the wing span. Furthermore, it is shown that the shedding of vortices from the propeller root, along with the resulting vortices on the lower side of the geometry, weakens the flap boundary layer as this flow is transferred through the cove area, consequently inducing flap flow separation. Overall, the findings provide valuable insights into propeller-wing-flap interactions, which had not been visualized before in this detail, yet emphasizing the need for further research to confirm and expand on these results.

I. Introduction

Renewed interest in propeller-driven aircraft has boosted research in propeller-wing aerodynamics. Turboprop aircraft are expected to increase in number due to rising demand for short-range aircraft and their higher propulsive efficiency compared to turbofan engines for short-range missions [1]. Additionally, the potential introduction of distributed electric propulsion (DEP) has led to greater interest in understanding the aerodynamic interactions between propellers, nacelles, wings, and flap systems. In a DEP system, multiple electrically driven propellers are placed along the aircraft wingspan. Recent examples of DEP projects are the X57 Maxwell aircraft [2] and Airbus SynergIE aircraft [3]. An advantage of DEP is its ability to improve high-lift performance compared to a wing with a single propeller. The work by Keller et al. [4] has shown a ≈12% improvement in $C_{L,max}$ due to the distributed propeller effect. While the results of Keller look promising, as of today, not all flow phenomena that occur in a tractor propeller-wing-flap (PWF) system are fully understood. Previous experiments by Duivenvoorden et al. [5] show a complex flow field at the flap of the experimental PWF setup, but the corresponding results alone do not lend themselves for a conclusive statement on the origin of observed flap flow phenomena. In fact, most publications that add a flap to a propeller-wing setup pay little attention to the flap flow but rather discuss overall high-lift performance by wing performance metrics, such as the research of Roosenboom et al. [6–8]. Furthermore, while recent DEP CFD simulations by Bongen et al. [9] exhibit good qualitative agreement with experimental measurements, the actuator disk approach employed in their study is unable to resolve the inherent unsteadiness of the slipstream. Simulations in which an unsteady approach is applied to resolve the time-accurate slipstream deformation and corresponding vortex systems in a DEP or conventional PWF system in order to analyze the complex flap flow are scarce in literature. The aim of the current study is to provide insights into the flow field around the entire tractor propeller-wing-flap configuration at high-lift and high propeller disk loading conditions by performing an unsteady RANS simulation. Special attention is given to the unsteady nature of the flow by quantifying flow fluctuations and comparing mean and time-accurate flow of primarily the flap flow field.

*MSc. Graduate, Delft University of Technology, Faculty of Aerospace Engineering, Flight Performance and Propulsion Section
†Ph.D. Candidate, Delft University of Technology, Faculty of Aerospace Engineering, Flight Performance and Propulsion Section
‡Assistant Professor, Delft University of Technology, Faculty of Aerospace Engineering, Flight Performance and Propulsion Section, AIAA Member, t.sinnige@tudelft.nl

II. Test Case Description

The geometry is based on the TUD-XPROP-S 6-bladed propeller and NLF-MOD22(B) airfoil with fowler flap. The goal of current setup is to maintain the same proportions as the work of Duivenvoorden et al. [5] while keeping the operational conditions of the wing-flap experiments of Boermans and Rutten [10]. This is done to maximize the Reynolds number, which is 600.000 in the experiments of Duivenvoorden et al. while still being able to use experimental data for validation. Furthermore, the uncorrected geometric angle of attack α is 8.0 deg in the work of Duivenvoorden et al. The complete setup of Duivenvoorden et al. has been enlarged by a factor of 2, except for the wing span, which has been enlarged by a factor of 1.63 to reduce mesh size. This approach allows for a qualitative comparison with the results of Duivenvoorden et al. while the operating conditions allow for a quantitative validation of a wing-flap only setup as further elaborated upon in section IV. CAD-files of the wing and propeller are available [11–13]. The case is meshed, solved and post-processed with Ansys® distribution 2020 R2.

A. Geometry

The physical TUD-XPROP-S 6-bladed propeller is scaled up with a factor of 2 to obtain a diameter D_p of 406.4 mm for this simulation. The wing has a flap-nested chord c of 600 mm. The span b is 2032 mm and equal to $5D_p$ to minimize the effect of the applied symmetry wall condition on the propeller slipstream development. The propeller is placed at approximately $0.85D_p$, 347 mm, upstream of the leading edge with its axis of rotation inclined downward with 5 deg with respect to the wing chord line. The propeller blade pitch $\beta_{0.7R} = 30$ deg. The flap deflection angle is 15 deg. At this setting, the optimal values ($(C_l/C_d)_{max}$) of dx, flap overlap, and ds, flap gap, as defined in Fig. 1, are $dx = 8\%c$ and $ds = 2\%c$ and hence applied in the current setup [10]. Figure 2 shows the corresponding airfoil.

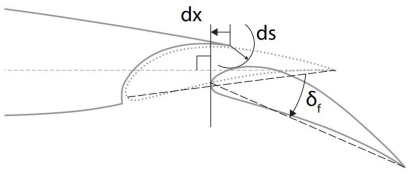

Fig. 1 Definition of flap deflection angle δ_f, overlap $dx[-]$ and gap $ds[-]$, the latter two normalized with chord. [5]

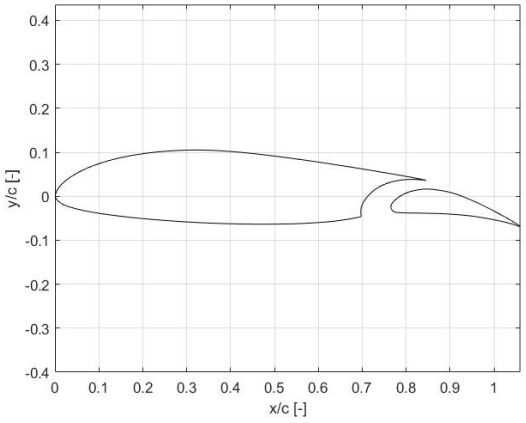

Fig. 2 Main airfoil and flap geometry of present work; $dx = 8\%c$, $ds = 2\%c$ and $\delta_f = 15$ deg

B. Operating conditions

The simulations are set up to represent a typical take-off condition, which includes both high wing lift and high propeller loading. The wing is set to an angle of attack α of 8.3 deg to match one of the settings tested by Boermans and Rutten [10] and facilitate comparison. The propeller operates at an advance ratio of J of 0.765, corresponding to a thrust coefficient T_c of 1.19 for this propeller [14]. T_c is defined as $T/(0.5\rho U_\infty^2 A)$, where T is propeller thrust, ρ air density, U_∞ far stream flow velocity and A the propeller disk area. A flap-nested chord-based Reynolds number of $2 \cdot 10^6$ is selected. The freestream Mach number M_∞ is 0.15 and ISA conditions at sea level are applied.

III. Numerical Methods

This section motivates the applied unsteady RANS approach, discusses the numerical settings followed by the setup of the computational domain and its grid.

A. Numerical setup

An unsteady RANS (URANS) approach is chosen because of its ability to provide complete flow field information at a Reynolds number higher than typically achieved in non-commercial wind-tunnel experiments. Current experimental results do not lend themselves for a conclusive statement of observed complex flap flow phenomena, but also are performed at too low Reynolds number at which flow phenomena occur that one does not expect at full scale conditions, for example laminar flow separation bubbles. CFD simulations can offer a solution by providing 3D insight into off-the-surface flow features to fully understand the flow mechanism at the flap of a propeller-wing-flap system while also increasing the Reynolds number of the setup to higher values compared to available experimental setups. URANS is highly preferred at high-lift wing-flap simulations and required for blade-resolved simulations [15–18]. Steady RANS simulations often converge to a wrong flow field at high angles of attack, while for this study LES was not feasible due to constraints on computational resources.

The simulation is solved by the Ansys® Fluent pressure-based solver which is recommended for low-speed aircraft aerodynamics [19]. The SIMPLE solution scheme and Spalart-Almaras (SA) turbulence model are selected. The SA model is robust, computationally cheap, and chosen most often in wing-flap CFD setups [16–18] and applied in many propeller-wing and propeller-wing-flap CFD research up to today (e.g. [4, 8, 9, 20–23]). The SA model is shown to accurately predict propeller-wing interaction effects when compared to experimental results [8, 22], but the model is prone to numerical dissipation and premature diffusion of vortex cores due to over-predicted eddy viscosity [8]. This is mitigated through the use of second-order temporal and spatial discretization, along with a high mesh resolution. The simulations are initialized from farfield conditions. Density is calculated by the ideal-gas law. Air dynamic viscosity is calculated in Fluent by Sutherland's Law. The time-step is equal to a propeller rotation of 2 deg.

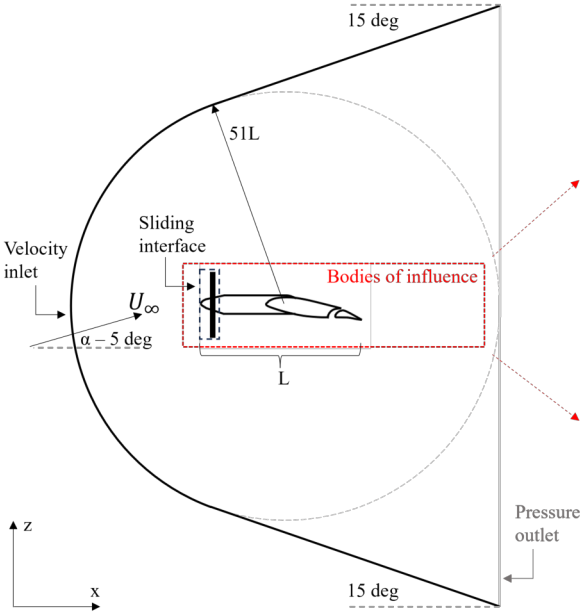

Fig. 3 Schematic representation of domain; not to scale.

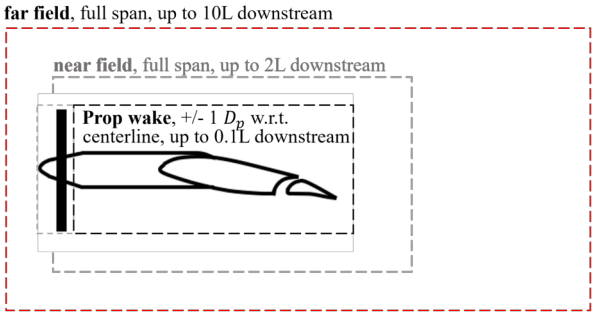

Fig. 4 Schematic representation of various mesh refinement regions (i.e. *Bodies of Influence*); not to scale.

B. Domain and grid

A bullet-shaped domain is set up as shown in Fig. 3. The curved surface is used as a velocity inlet while the downstream surface is selected as a pressure outlet. The domain extends at least 50 body lengths. A constant pressure boundary condition is applied to the outlet. The full propeller geometry is modeled to include the root-nacelle interaction of the propeller blade and to obtain a real viscous propeller wake, leading to an accurate prediction of the propeller slipstream velocity field [6, 8, 24–26]. A no-slip boundary condition is applied at the full propeller geometry, wing, and flap. The side-walls of the domain are defined as symmetry planes.

A hybrid-grid is implemented, consisting of an unstructured far-field with semi-structured inflation layers with a thickness of 36 layers to resolve the boundary layers on all surfaces. The first layer height is $6 \cdot 10^{-6}$ m and a growth rate of 1.15 is applied. The average y^+ is 0.5 while its maximum is 1.6. A polyhedral mesh is selected in the Fluent software due to its lower RAM requirements and reduced convergence time when compared to default tetrahedral meshing, while accuracy is not adversely affected [27]. The rotating propeller is implemented by a sliding mesh approach. Figure 4 shows a schematic representation of multiple mesh refinement regions in order to minimize numerical diffusion of flow structures of interest. The smallest cells (0.0025) m are found in the propeller wake refinement area.

To verify correct meshing and solving techniques and increase the credibility of the final simulation, two additional less complex RANS simulations are performed of a wing-flap and prop-off setup. Figure 5 shows the geometries of all setups. The total number of cells ranges from 117 million for the wing-flap case up to 190 million for the prop-on case.

The URANS approach combined with a high mesh resolution results in long computation times, with the prop-on simulation requiring 82,000 CPU hours and a turn-around time of two months. Considering the time span of this study, a mesh dependency analysis is not performed.

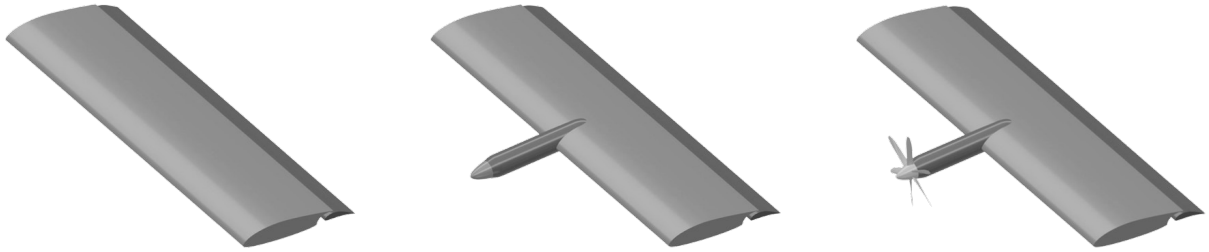

(a) Wing-flap (RANS) **(b) Prop-off (RANS)** **(c) Prop-on (URANS)**

Fig. 5 Overview of CFD configurations

IV. Verification and Validation of Numerical Results

In this section, the verification and validation approach and results are discussed. Validation data of the full propeller-wing-flap setup are not available at the specific operating conditions. The wing-flap setup is validated by experimental results of Boermans and Rutten [10]. Only a qualitative comparison is made with the work of Duivenvoorden et al. [5] and the Lattice-Boltzmann simulation results of Ribeiro et al. [28].

A. Wing-Flap

The wing-flap case is primarily validated by chordwise pressure coefficients and C_l results of Boermans and Rutten [10]. Standard low-speed wind tunnel corrections have been applied in their results. A C_l of 2.12 is obtained, closely aligning with the experimentally obtained C_l of 2.11. Figure 6 shows good agreement between the experimentally obtained chordwise C_P distribution and the CFD results of this study, with the exception of two regions on the suction side of the flap, highlighted by the red boxes. These local pressure distributions originate from the separated flow of the main element's cove area, interacting with the pressure distribution near the flap surface. Similar structures and under-resolvement of the extremes in these regions are seen in the research of Ribeiro et al. [28] when assuming fully turbulent flow, yet better matching CFD results were obtained when flow transition was included in their setup. It is therefore concluded that the mismatch between experimental and present CFD results is caused by the fully-turbulent RANS assumption of the present setup.

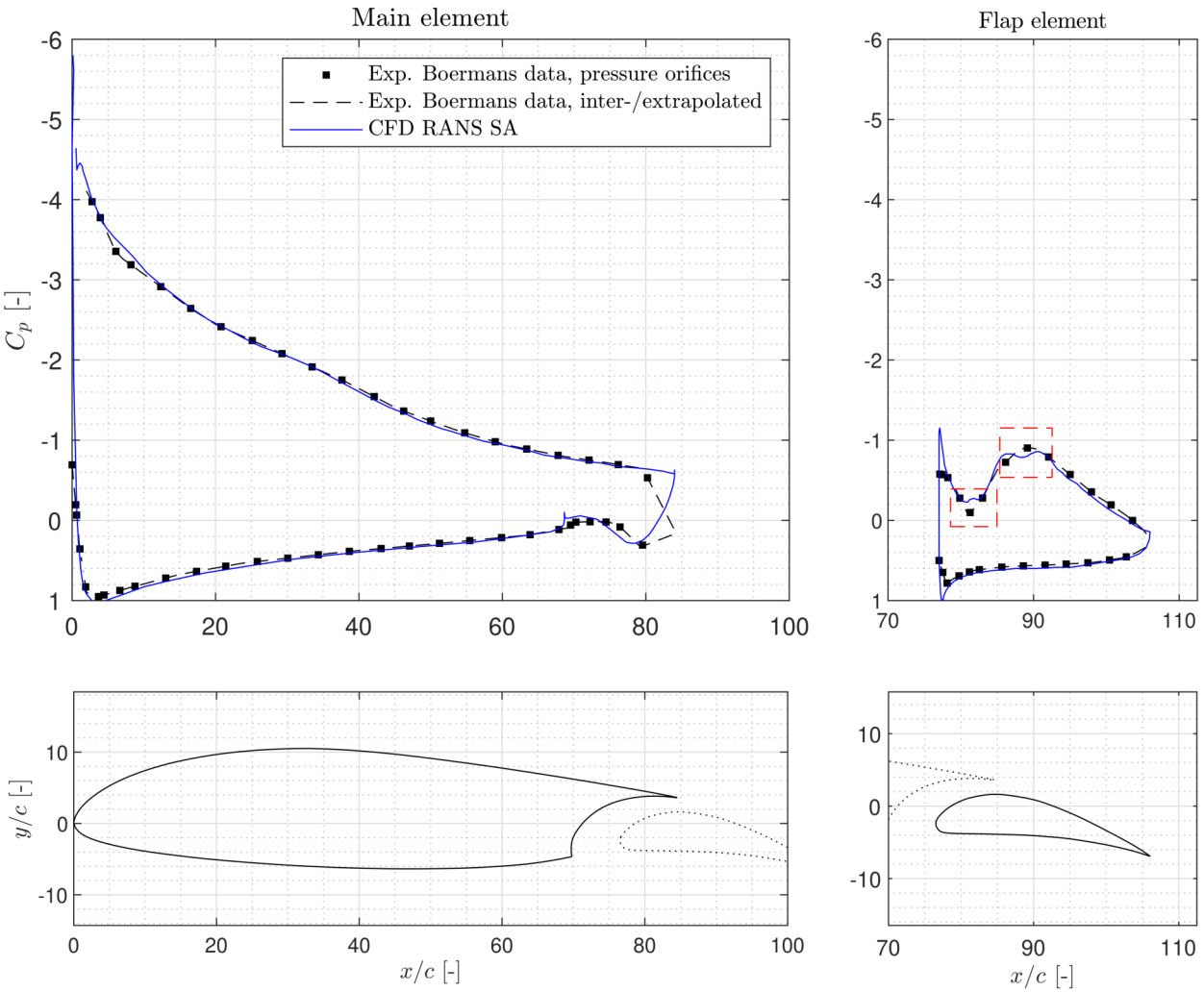

Fig. 6 Chordwise pressure coefficient validation by experimental Boermans and Rutten. Experimental wind tunnel data from Ref. [10]. (The inter-/extrapolation of the experimental data is performed by Boermans and Rutten.)

Furthermore, the C_d of current research, 302 drag counts, exceeds the C_d of Boermans and Rutten of 260 drag counts with 16.2%. This error did not reduce with additional mesh refinements and can be explained by the fully turbulent flow assumption used in the RANS simulations. Boermans and Rutten did not apply forced transition in their setup while laminar separation bubbles are observed. In fact, the NLF-Mod22 airfoil is designed to postpone transition, reducing drag by maintaining laminar flow as long as possible. The wing-flap results are deemed sufficient despite some minor differences in pressure distributions and drag due to boundary conditions.

B. Prop-Off: Wing-Flap + Nacelle

In the prop-off case a nacelle and hub are added to the wing-flap setup. The C_l slightly reduced from 2.12 of the wing-flap setup to an integrated lift coefficient C_L of 2.06 in present case due to local suppression of the leading edge suction peak by the nacelle. A reduction in C_L of approximately the same magnitude is seen in the results of Duivenvoorden et al. [5], from 1.98 to 1.90. The lower lift values from the experiment are related to a low Reynolds number of $6 \cdot 10^5$, boundary layer tripping to force boundary layer transition and spanwise variations. In respective research lift and pressure drag measurements are based on two rows of pressure taps at spanwise locations $y = \pm 0.35 D_p$ relative to the nacelle centerline. The spanwise C_l and pressure drag coefficient $C_{d,press}$ distribution of current work is

shown in Fig. 7 including a depiction of the experimental pressure taps position. Duivenvoorden et al. [5] obtained a negative pressure drag caused by an increased suction peak near the wing-nacelle intersection. The present work confirms that the pressure taps are positioned very close to this suction peak, resulting in a local negative pressure drag.

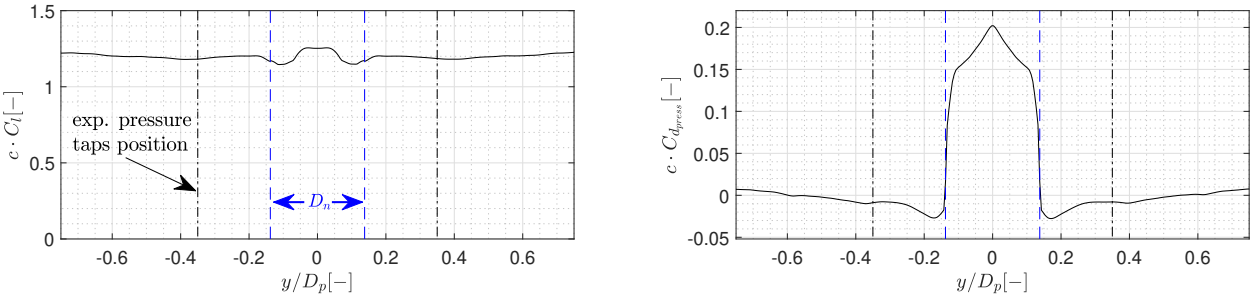

Fig. 7 Spanwise lift (left) and pressure drag (right) distributions of prop-off RANS simulation. Dotted blue lines indicate diameter of nacelle D_n. Dotted black lines indicate location of pressure taps of Duivenvoorden et al. [5]

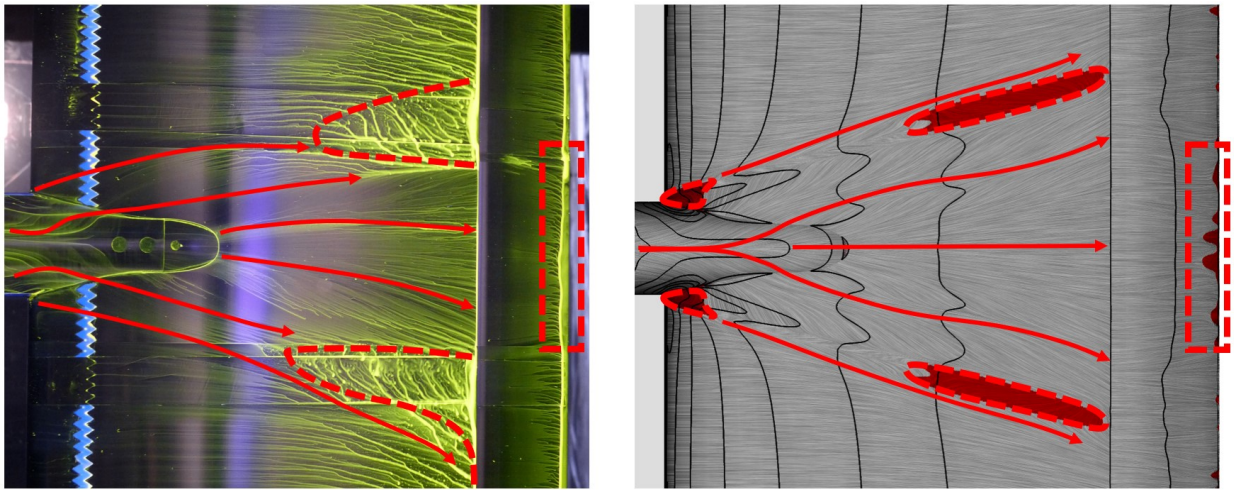

Fig. 8 Comparison of experimental oil flow visualizations at α 8.0 deg (left) [5] with current simulation at α 8.3 deg (right). Simulation results are overlapped with surface C_p contours in black and regions of reversed flow ($-x$ surface shear) colored in red.

Figure 8 shows a comparison between the oil flow visualizations of Duivenvoorden et al. [5] and current results. In general, the CFD surface shear lines show similar trends as the experimental flow visualizations considering that the experimental setup was mounted vertically, hence gravity has effect on the oil flow. Areas with flow separation are marked by red dashed lines. The simulation sufficiently predicts the local flow separation regions at the main wing element considering the complex flow and applied CFD methodology. The experiment shows slightly increased flap trailing edge stall downstream of the nacelle, which is also evident in the CFD results. Additionally, the simulation predicts flow separation near the nacelle-wing intersection, consistent with the findings of Qui et al. [29]. While this separation is not observed in the experimental results of Duivenvoorden et al. in Fig. 8, a distinct leading edge separation bubble is present at an angle of attack of 10 deg in the corresponding report [5]. This suggests that the CFD setup predicts the main relevant phenomena. Considering the small differences in operating conditions and RANS limitations, the results are well accepted.

C. Prop-on

The prop-on case represents the full setup. Figure 9 shows the convergence history of C_L, C_D and T_C of this simulation. A total of 60 propeller rotations, equal to a 0.36 s total simulated time and 4800 time steps, are successfully simulated to allow the flow field to establish and converge to a quasi-steady solution, similar to the approach of

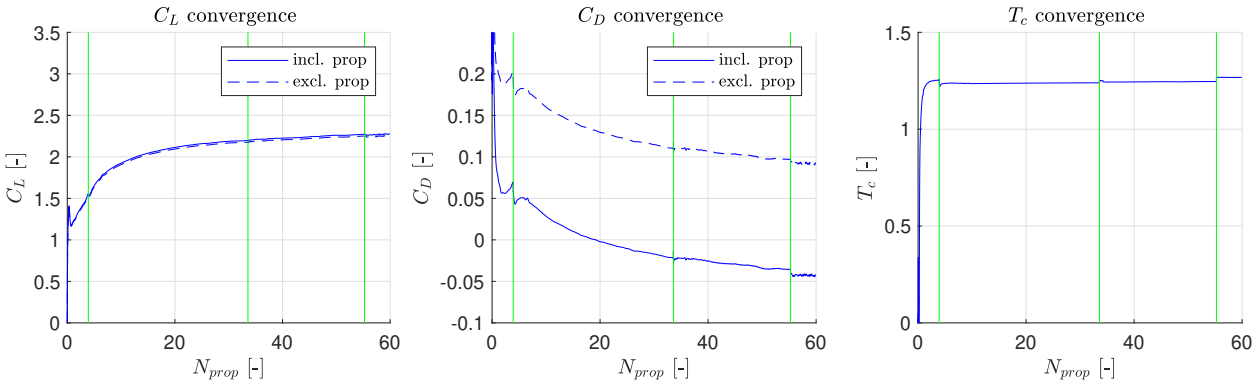

Fig. 9 Convergence history of forces for the prop-on case. *'incl. prop'* shows the forces of the full geometry, *'excl. prop'* shows the forces of the stationary mesh components only. The green lines indicate time stamps where solver settings are adjusted, in the following sequence: application of second-order temporal discretization at, wake mesh refinement, and application of second-order spatial discretization.

Roosenboom et al. [8]. During the last 3 propeller rotations, data sampling is applied to obtain time statistics of the unsteady flow field. A T_C of 1.24 was expected based on extrapolating data of earlier performed experimental measurements at zero angle of attack [30]. A slightly higher value of 1.267 is obtained by analyzing the forces on the propeller and spinner only. The non-zero angle of attack leads to an azimuthal variation of inflow conditions. The down going blade experiences a larger increase in angle of attack and dynamic pressure than the reduction of angle of attack and dynamic pressure for the up going blade, resulting in increased thrust. Furthermore, the upwash of the wing on the propeller imposes a local increased angle of attack at the propeller plane, resulting in an additional thrust increase [31, 32]. The obtained T_C is therefore accepted.

The slipstream deformation is a direct result of the propeller-wing interaction and therefore an important metric of current work. To verify correct propeller slipstream development, the current results are compared with experimental wake rake measurements of Duivenvoorden et al. [5] and the Lattice-Boltzmann simulation results of Ribeiro et al. [28] in Fig. 10. The experimental wake rake is located 1 chord length downstream of the flap trailing edge. A plane at the same location is implemented by Ribeiro et al. (Fig. 10a) and in the current study during CFD post-processing (Fig. 10c). On these planes, the total pressure coefficient is shown, defined as $C_{p_t} = (p_t - p_\infty)/q_\infty[-]$, where p_t is the local total pressure, p_∞ the freestream static pressure, and q_∞ the freestream dynamic pressure. As a propeller adds total pressure to the flow, areas of $C_{p_t} > 1$ are indicative of the propeller slipstream and used to validate that current research accurately solves the downstream slipstream deformation. In general, very good agreement with Duivenvoorden et al.

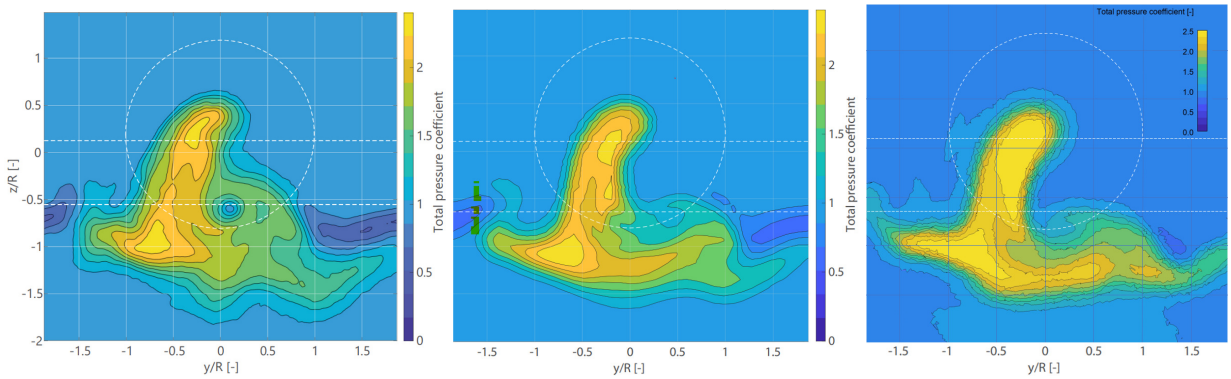

(a) Ribeiro [28], (Lattice-Boltzmann) $\alpha = 8.0$ deg, $J = 0.8$, $\delta_f = 15$ deg

(b) Duivenvoorden [5] (experimental) $\alpha = 8.0$ deg, $J = 0.8$, $\delta_f = 15$ deg

(c) Current research (URANS) $\alpha = 8.3$ deg, $J = 0.765$, $\delta_f = 15$ deg

Fig. 10 Total pressure coefficient plane, 1 flap-nested chordlength downstream of flap trailing edge ($x/c = -2$). Dashed white lines indicate propeller disk, main wing leading edge and flap trailing edge.

[5] is observed considering the small differences in operating conditions. The main difference is the slightly higher total pressure coefficient in the center of the typical inverted T-shaped slipstream due to the lower advance ratio, hence increased thrust coefficient, of the CFD setup. It is assumed that for the same reason, the bottom half of the slipstream at +/- 1.5 y/R shows a slightly larger deformation in the spanwise direction compared to Duivenvoorden et al. [5], although the slipstream in these regions interacts with the wing wake, challenging the identification of the propeller slipstream edge. Based on the total pressure coefficient contours, current methodology does better capture the slipstream deformation compared to the Lattice-Boltzmann simulation but this comes with the price of high computational costs [33]. Also for this case the surface flow field is examined. Good agreement is observed between the CFD shear stress contours and the oil flow visualizations in Fig. 11. The experimental results of Duivenvoorden et al. [5] show two regions of separated flow, located just outside the area influenced by the propeller slipstream, depicted by numbers I and II in Fig. 11. These flow reversal regions are sufficiently resolved by the URANS simulation, including details such as the slightly earlier onset of flow reversal on the propeller blade-up side (region II) compared to the blade-down side (region I). The experimental results also show two flow reversal regions on the flap, III and IV. The simulation shows areas with flow reversal in the same regions, but in a more chaotic pattern. Overall, present CFD results show similar flow compared to the experimental results, meaning the relevant aerodynamic phenomena are resolved, which is sufficient for the purposes of this paper.

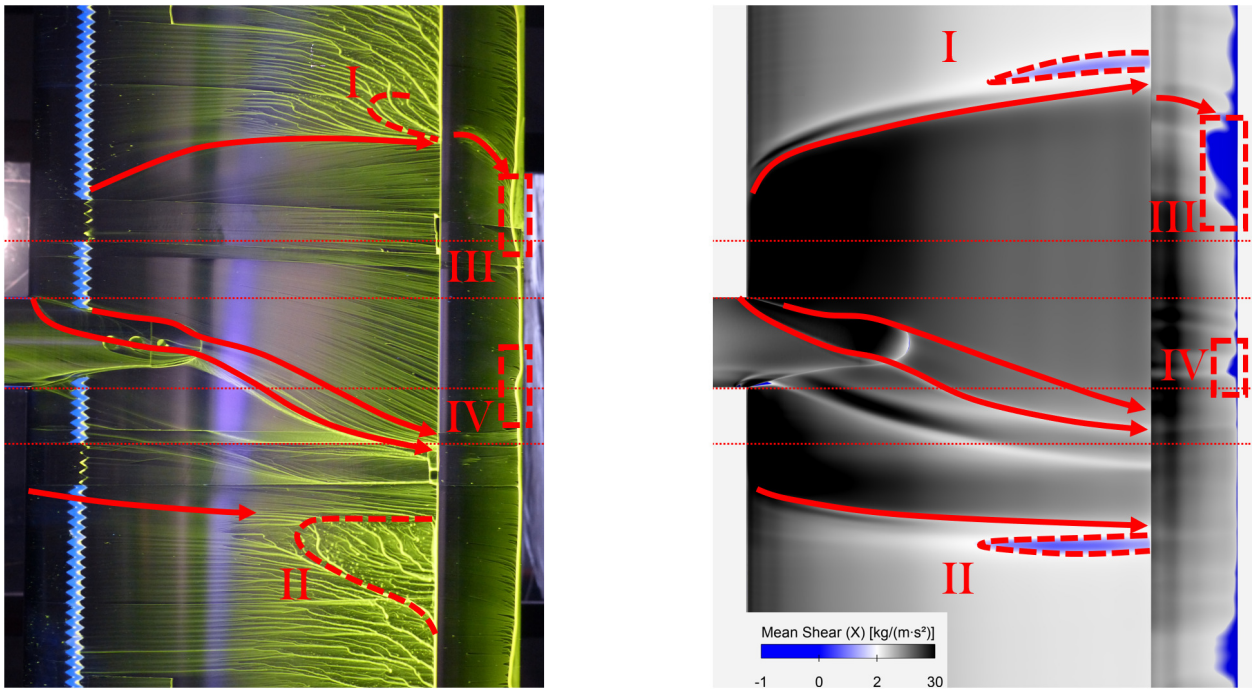

Fig. 11 Comparison of experimental oil flow visualizations at α = 8.0 deg and J = 0.8 (left) [5] with current simulation at α = 8.3 deg and J = 0.765 (right).

V. Results

This section presents the results of the prop-on URANS simulation. Section V.A provides an overview of the volumetric flow field, focusing on the region up to the main wing trailing edge and including a decomposition of the flow field to identify concentrated vortex cores, their trajectories, and their influence on the surface flow. With a good understanding of the flow field established up to the main element trailing edge, the flap flow is analyzed in Section V.B. Two separated flow regions are identified at the flap, which are further discussed in Sections V.B.1 and V.B.2

A. Propeller, nacelle and main wing flow

The propeller slipstream is initially examined by Fig. 12. The geometry is colored by wing shear, with regions of negative x-shear in red to identify flow separation. The propeller experiences separated flow at its trailing edges due to the high angle of attack and the low advance ratio of 0.765 compared to the optimal propeller advance ratio of 1.0.

Iso-surfaces of positive Q-criterion are shown, colored by x-vorticity to identify the rotational direction of shed

vorticity. Multiple vortex systems are clearly visible, such as the propeller tip vortex, near-root vorticity, and the vortex systems originating from the wing-slipstream interaction in Fig.12a. Figure 12b provides a side view from the upgoing side. The propeller tip vortices bend around the wing's leading edge, similar to the findings of Ribeiro et al. [28]. Furthermore, Fig. 12b shows how the entire tip vortex folds into the pressure side of the wing while remaining more perpendicular to the wing on the suction side. The high angle of attack setting leads to high wing circulation and higher flow velocity on the upper side, preserving the clear structures of the tip vortices. The pressure side, however, experiences low wing circulation and thus lower flow velocities, leading to vortex-vortex interactions and breakdown of the tip vortex helix.

On both the blade-up and blade-down sides of the main element, the wrapping of the tip vortices around the leading edge results in an initial widening of the slipstream away from the nacelle centerline, likely due to a vortex imaging effect [34]. This interaction produces two distinct vortices, marked by red arrows in Fig. 12a. Two regions of separated flow at the main element of Fig. 11 are marked with white arrows in Fig. 12a. These local flow separation zones likely result from boundary layer thickening, just outside of the propeller slipstream, caused by the orientation of the distinct vortices. The separated region on the upgoing side is slightly more intense and extends further forward than on the opposite side, also visible in Fig. 11. An explanation could be the upwash on the propeller's blade-up side, which leads to a generally higher leading-edge angle of attack than on the blade-down side.

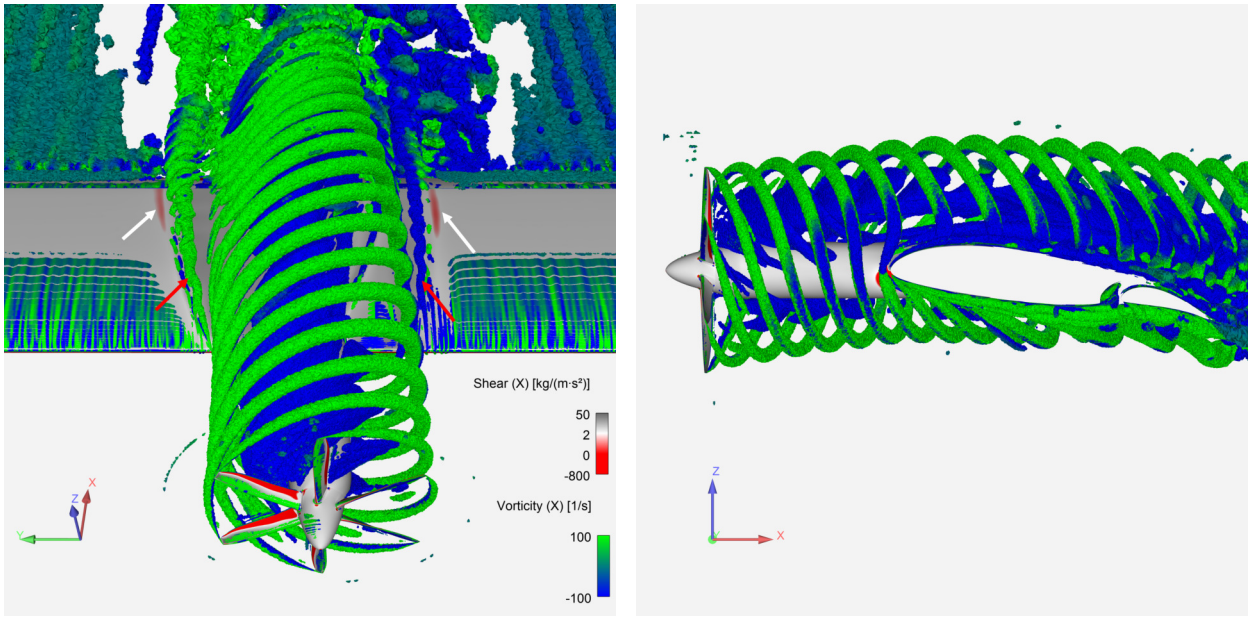

(a) Frontal view. White arrows depict flow separation regions at main element suction side. Red arrows depict vortices from tip vortex - leading edge interaction.

(b) Side view.

Fig. 12 General impression of 3D flow field by positive normalized 0.001 Q-criterion iso-surface, colored by x-vorticity, and surface shear stress in upstream x-direction. Red areas indicate areas of negative x-shear.

Figure 13a shows contours of the total pressure coefficient at the trailing edge of the main element to further decompose the various vortex systems. A low total pressure coefficient could indicate the presence of a vortex core. The viscosity in the vortex core dissipates energy, reducing C_{p_t}. A total of six bundles of streamlines are released in regions of low C_{p_t} to identify the path and origin of the possible total pressure deficits, as shown in Fig. 13b and Fig. 13c.

The yellow streamlines in Fig. 13b correspond to the down-going side vortex originating from the interaction between the blade-down side of the propeller slipstream edge and the main wing. The vortex imposes an upwash at the outboard, low momentum, wing boundary layer as seen in Fig. 13a at y/r=−1.5. This leads to boundary layer thickening, accelerating flow separation.

Vortex shedding at the propeller root sections generates two vortices, represented by the red and purple streamlines in Fig. 13. The red streamlines originate from the root sections on the blade-up side of the propeller. These streamlines cluster to a condensed counterclockwise (negative x-vorticity) oriented vortex. This induces a local spanwise flow

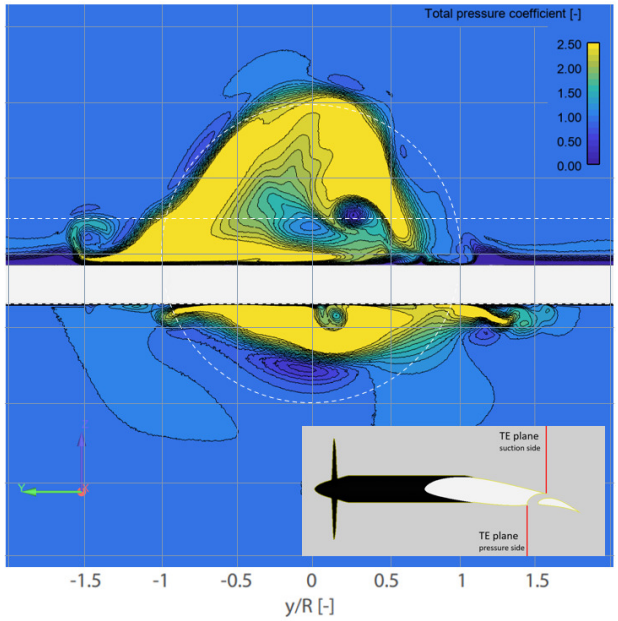

(a) Main wing trailing edge C_{p_t}

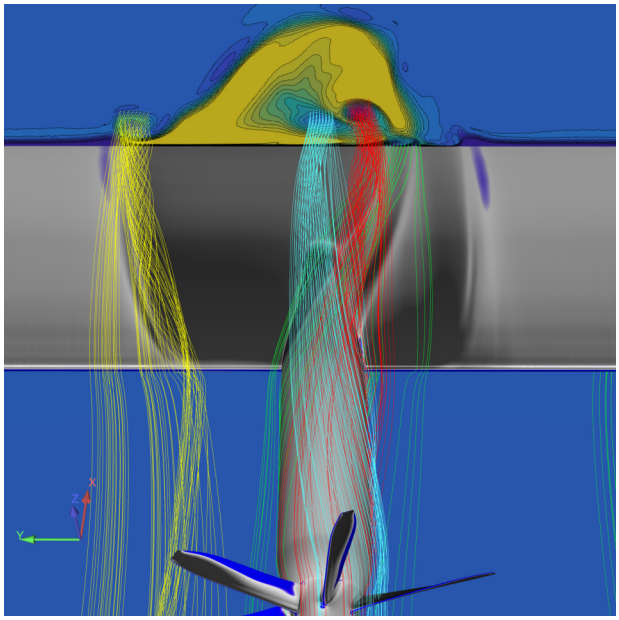

(b) Wing suction side

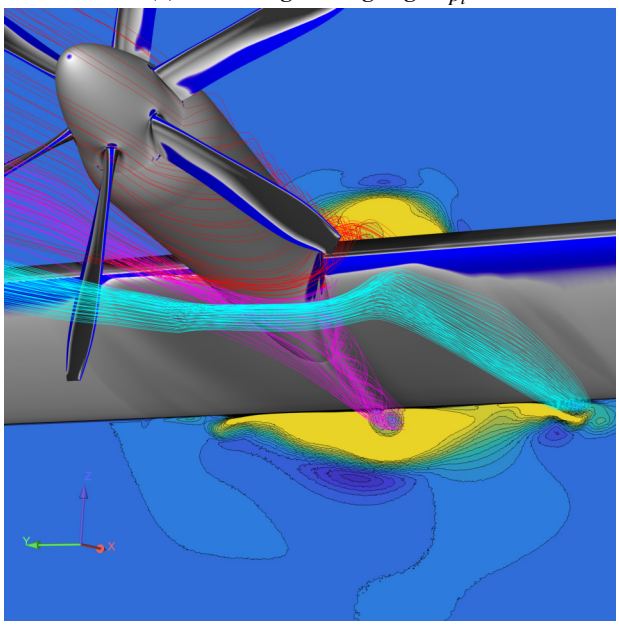

(c) Wing pressure side

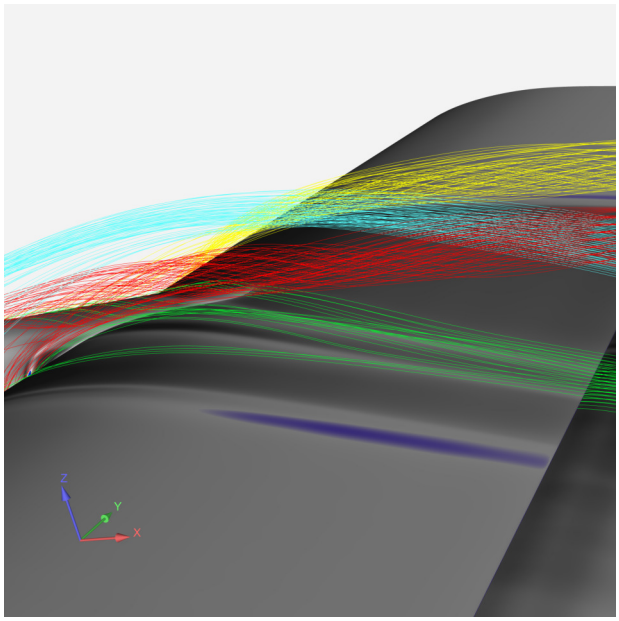

(d) Wing suction side

Fig. 13 Mean-streamlines calculated from low C_{p_t} areas in Fig. 13a to identify total pressure deficits and possible vortex cores. Streamlines are grouped and colored by region to distinguish their trajectories.

component to the blade-up side, away from the centerline, on the upper side of the main element denoted by the green streamlines in Fig. 13b. A similar roll-up of flow into a vortex is observed for the purple streamlines, but being on the lower side of the wing, it imposes a spanwise flow component towards the nacelle centerline.

The complex flow results in a large spanwise variation in lift, shown in Fig. 14. In this figure, the black line shows the mean spanwise lift distribution, while the rose-colored areas show the Root Mean Square (RMS) variation of the lift distribution due to the unsteady slipstream flow. Figure 14a shows the spanwise lift distribution of the full geometry. The blade-up side shows a higher lift compared to the blade-down side due to the upwash of the propeller. The largest variations in lift, up to +/- 7.4% with respect to the mean lift, are seen at the slipstream edges due to the tip vortex

interaction with the main wing, in which the upgoing side exhibits slightly larger fluctuations than the downgoing side. Near the centerline of the nacelle, at +/- r_n, only minimal variations are observed.

In Fig. 14b and Fig. 14c the spanwise lift distributions are split up in the main element, respectively the flap. Note how both sub-figures have the same scale on the vertical axis. The flap encounters far less intense fluctuations compared to the main element. Spanwise contours of x-velocity fluctuations ($U'_x/\bar{U}_x$) in Fig. 15, indicate that the fluctuations in spanwise lift primarily originates from velocity fluctuations on the pressure side of the wing. This is attributed to vortex-vortex interaction and the closer proximity of the propeller tip vortices to the pressure side compared to the suction side. Figure 15a illustrates the region in the middle of the blade-up side slipstream, where vortices from the lower side of the geometry approach the surface, resulting in highly fluctuating flow. The cross-sections of Fig. 15a, 15b and 15c are all located within the propeller slipstream suction side part, but only minimal fluctuations approach the

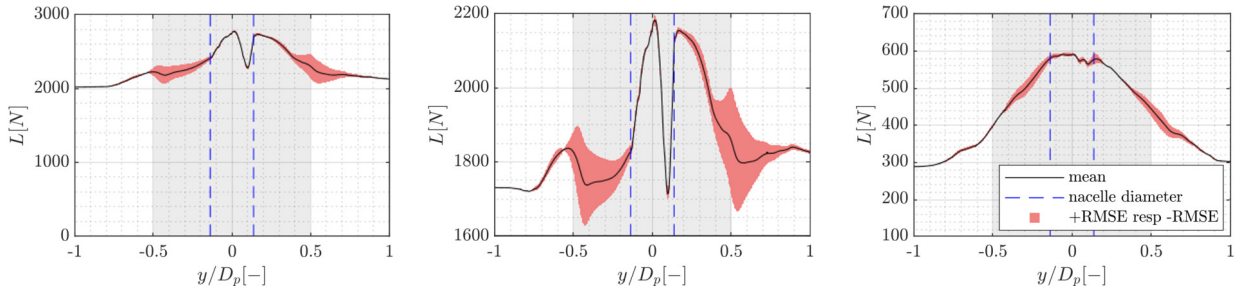

(a) full geometry **(b) spinner, nacelle, main wing only** **(c) flap only**

Fig. 14 Spanwise lift distributions and RMS variation.

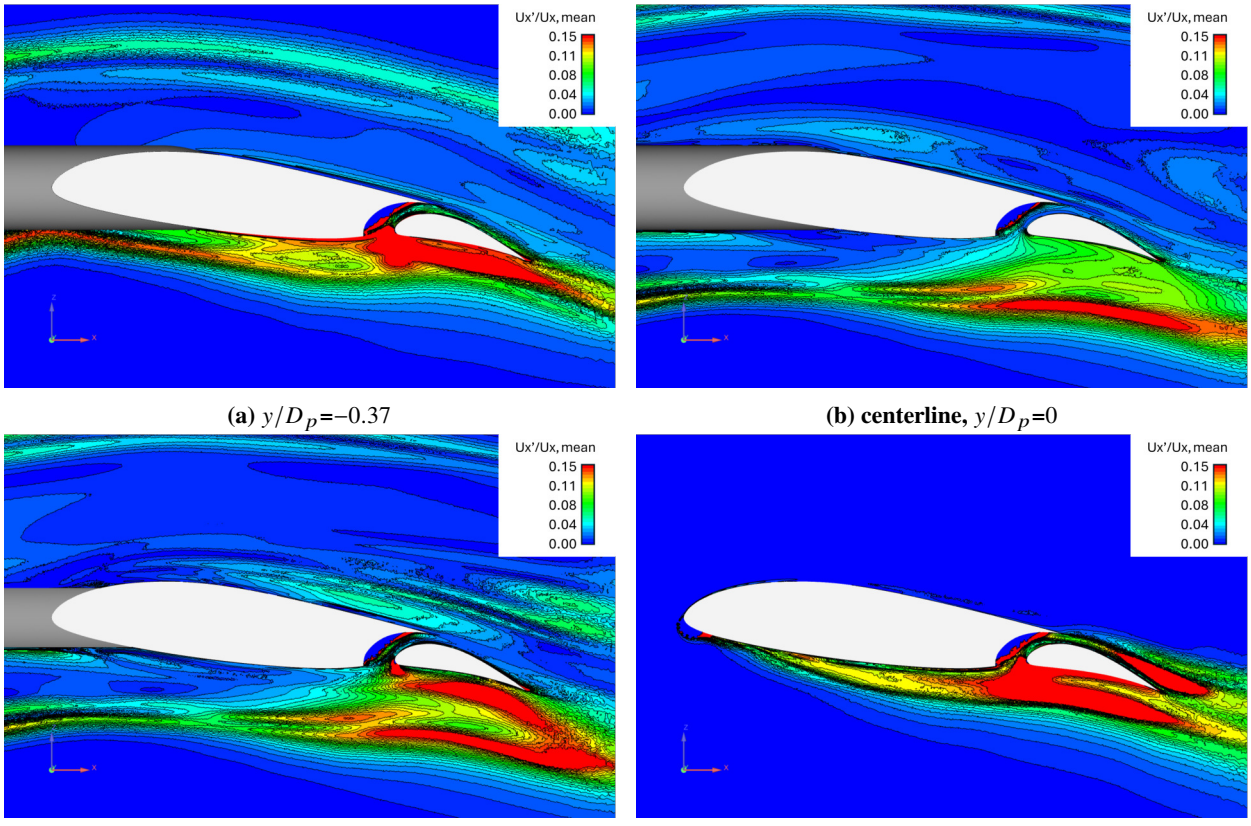

(a) y/D_p=−0.37 **(b) centerline,** y/D_p=0

(c) y/D_p=0.10 **(d)** y/D_p=0.63

Fig. 15 Velocity fluctuations at various y/D_p. RMS variation x-velocity divided by mean x-velocity $U'_x/\bar{U}_x$

upper surface of the main element. Figure 15d is positioned outside the propeller slipstream on the suction side but within the propeller slipstream on the lower side of the geometry as a result of slipstream deformation. While the upper side of the main element does not experience any fluctuating flow, the flap section is entirely immersed in fluctuating flow through the cove area.

B. Flap flow

The complex interaction between the propeller, nacelle, and main wing influences the downstream flow in the flap region. The flap boundary layer flow is dominated by the main element pressure side flow, where flow fluctuations due to low flow velocity and resulting vortex-vortex interactions are observed. This fluctuating flow transfers to both the upper and lower surfaces of the flap.

This unsteady flow is clearly visible at spanwise location y/D_p=0.63 as shown in Fig. 15d and the zoom-in of Fig. 16. Due to the propeller slipstream deformation, at this cross section, the lower side of the main wing is inside the propeller slipstream, while the upper side is outside of it. Figure 16b shows the progression of unsteady flow through the cove area and reaching the upper surface of the flap.

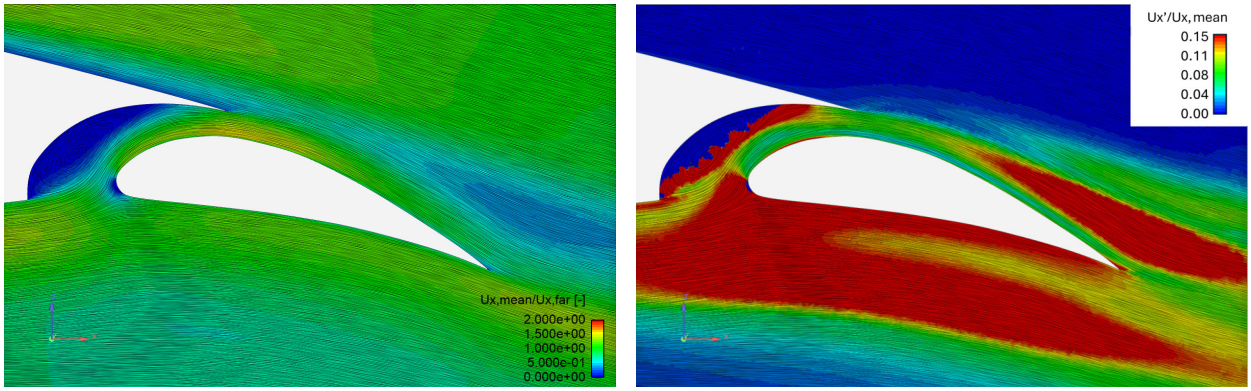

(a) $\bar{U}_x/U_\infty$ **(b)** $U'_x/\bar{U}_x$

Fig. 16 Zoom-in at y/D_p=0.63 of mean velocity and fluctuations, including mean velocity line integral convolution visualization.

The unsteadiness of the flap flow is further quantified by the surface friction coefficient and its fluctuations. Figure 17 shows the influence of this unsteadiness on the spanwise surface friction coefficient in downstream direction $C_{f,x}$. The first row of this figure shows the main wing spanwise $C_{f,x}$, slightly upstream of the cove area. The next 4 rows show the flap spanwise $C_{f,x}$ near its leading edge, 31.3%, 65.39% x/c_{flap} and near its trailing edge. At the main wing, the pressure side shows significant variation in $C_{f,x}$ due to vortex-vortex interaction, while the suction side only shows marginal variations as most vortical structures on the suction side are maintained in downstream direction. The fluctuations at the main wing pressure side transfer to the flap upper and lower surfaces, leading to large fluctuations in $C_{f,x}$ at both sides of the flap. The fluctuations are seen to reduce downstream on the suction side, while the lower surface shows fairly constant fluctuation magnitude up to the trailing edge.

The increase of flow momentum by the propeller is visible by the increased friction coefficient within the slipstream and reduces, in general, flow separation on the flap. However, Fig. 11 shows two distinct flow separation regions, areas III and IV. The mechanisms underlying these separation regions are investigated in the next sections.

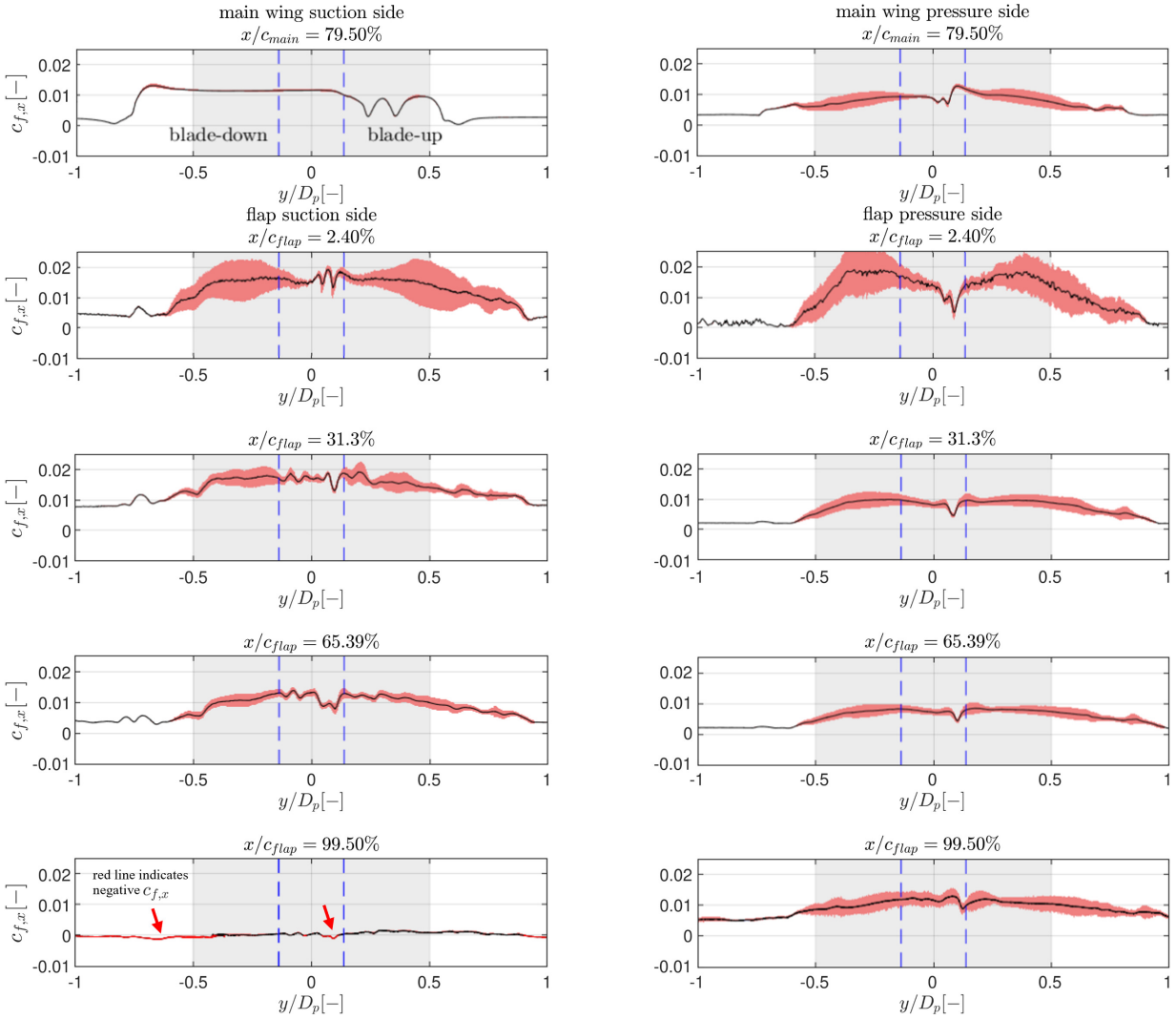

(a) Suction side **(b) Pressure side**

Fig. 17 Spanwise surface friction coefficient distribution and RMS variation at main wing (top row) and flap (4 last rows) suction and pressure sides. Rose colored areas indicate the magnitude of the fluctuations by RMS.

*1. **Minor flap flow separation area, area IV***

The first area of separated flow at the flap to be discussed is positioned between $y/D_p = 0.02$ to 0.10, just to the blade upgoing side from the nacelle centerline. Figure 18 shows streamlines through the separated region. In Fig. 18b, the Q-criterion iso-surface shows that the streamlines rotate around the vortex originating from the propeller root vorticity, discussed earlier by the purple streamlines in Fig. 13c. The flow corresponding to this vortex transfers through the cove area to the upper side of the flap, although the actual vortex disintegrates from the cove onward. Figure 18a shows that the vortex is positioned relatively far from the main element while the streamlines are within the flap boundary layer. The flow corresponding to the vortex shows a low total pressure coefficient at the trailing edge of the main wing's pressure side in Fig. 13a. As internal viscosity reduces the energy of vortex flow prior to the cove area, the authors believe that this flow weakens the flap boundary layer by the transfer of this flow through the cove area, consequently inducing flow separation. However, this negative effect on high-lift performance should be placed in context: if the local dip in lift can be avoided in future aircraft design, the expected increase in lift of the slipstream-affected flap region is only an insignificant $\approx 0.15\%$ based on integrating the spanwise flap lift distribution. The lift increase of the full geometry could be different as the modified flap flow could affect the aerodynamics of the full geometry.

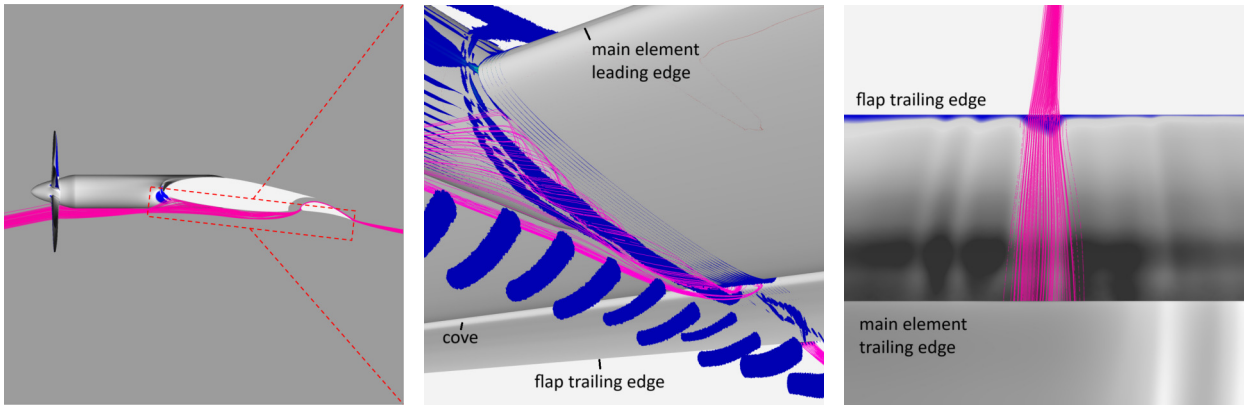

(a) Side view, upgoing side **(b) Zoom-in pressure side. Streamlines and Q-criterion iso-surface** **(c) Zoom-in flap suction side. Streamlines and surface shear.**

Fig. 18 Streamlines corresponding to minor flap separated flow region at y/D_p=0.02 to 0.10, originating from the pressure-side vortex system (purple streamlines) of Fig. 13c.

*2. **Major flap flow separation zone, area III***

A similar approach is taken to investigate the origin of the major flow separation zone, area III of Fig. 11 and Fig. 20a. Streamlines are calculated from a plane located downstream of the major separated flow region, shown in Fig.19. This flow also originates from the lower surface of the main element, close to the wing surface and near the path of the propeller tip vorticity. The streamlines clearly show an inboard deflection of the flow near the separated area. C_p contours provided in Fig. 20 reveal a low static pressure area at the middle of the flap, caused by the high-momentum slipstream flow from primarily the upper side of the geometry. This low-pressure region induces an inboard-directed pressure gradient, which strengthens the spanwise deflection of the streamlines next to the overall slipstream shift at the flap to the blade-up side. These mutually reinforcing factors likely contribute to the pronounced inboard deflection of the streamlines as they approach the separated region. Furthermore, the deflection of the streamlines through a low pressure region with increased adverse pressure gradient thickens the local boundary layer and promotes flow separation.

The origin of the flow separation region is further examined by considering the vortex systems on the suction side of the wing, originating from the propeller tip vortices and main wing - slipstream intersection. The deformed propeller tip vortices do not reach the flap surface as discussed earlier. However, any influence they exert on the flap is expected to be beneficial (counteracting flow separation), due to the local vorticity induced downwash component on the flap. This further emphasizes the conclusion that the flow over the flap is primarily influenced by the part of the propeller slipstream that flows on the lower side of the main wing.

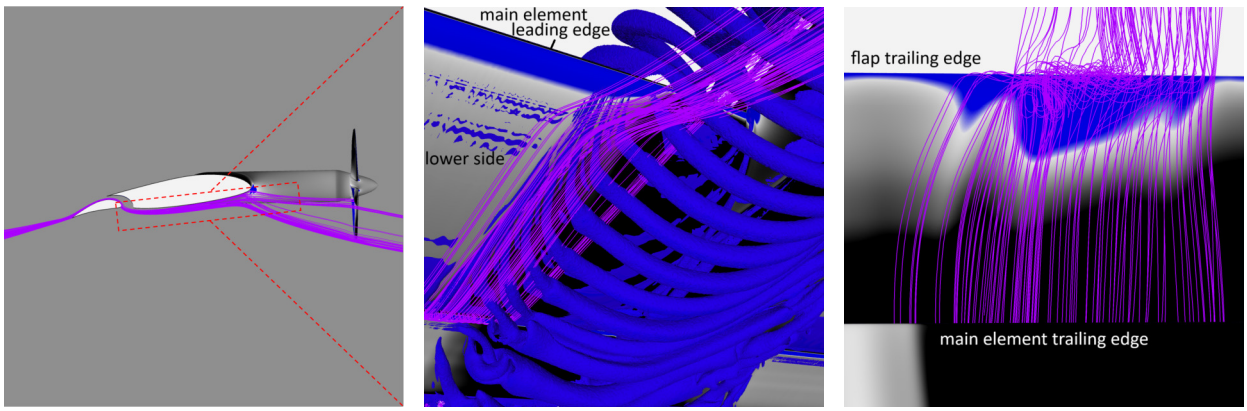

(a) Side view, starboard side **(b) Zoom-in pressure side** **(c) Zoom-in flap suction side**

Fig. 19 streamlines trajectory to major flap suction side separated flow region at y/Dp=-0.62.

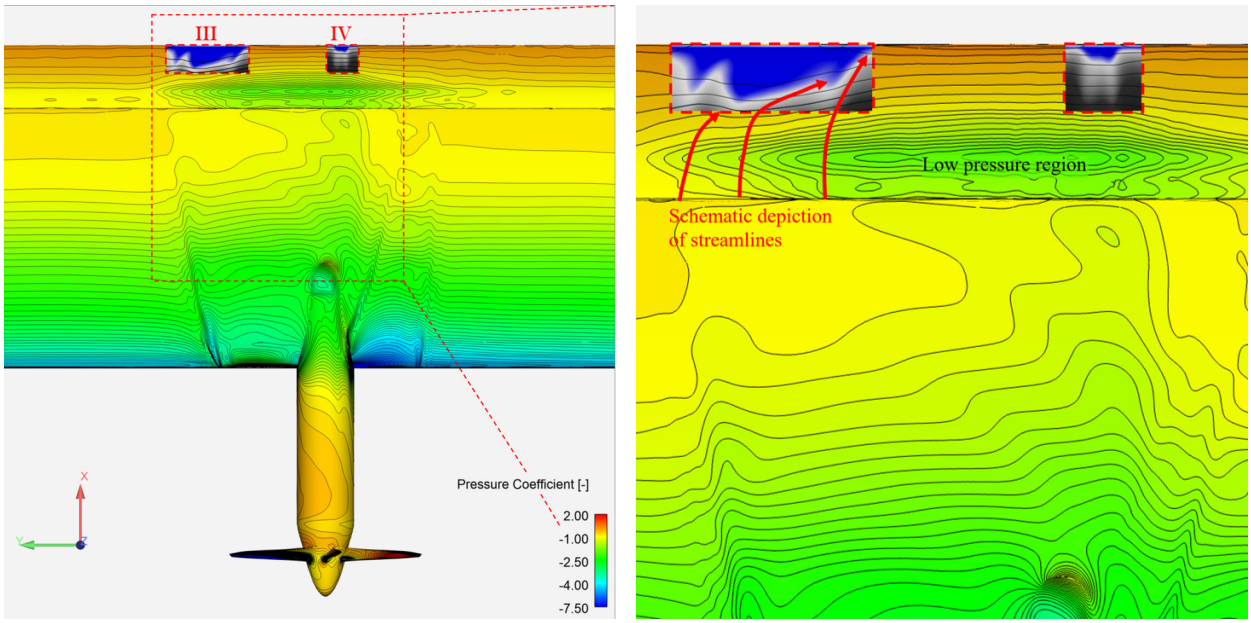

(a) Overview **(b) Zoom-in**

Fig. 20 Pressure coefficient contours locally overlapped with surface shear contours

In this section it is shown that the overall flap surface flow field is dominated by the flow from the pressure side of the main element. The flow corresponding to the major flow separation region, area III, is low energetic and originates from the propeller slipstream edge. The vortex system originating from the upper side of the main element should have, if any, a favorable effect on the flap, next to the high momentum flow of the propeller slipstream. However, the flap boundary layer still separates, underlining that the flap boundary layer is dominated by the flow from the pressure side of the main element and spanwise flow variations imposed by the slipstream deformation, affecting flap performance. The major flap flow separation region is shown to be complex and not easy to decompose, and a complete insight is not achieved in this paper. Additional research is necessary to comprehensively analyze the flow and its interaction effects before a definitive conclusion can be reached.

VI. Conclusion

An unsteady RANS simulation using the Spalart-Allmaras turbulence model is performed on a propeller-nacelle-wing-flap configuration at a chordwise Reynolds number of 2 million at an angle of attack of 8.3 deg. The configuration includes a six-bladed propeller at an advance ratio of 0.765 with a thrust coefficient of 1.267, and a single-slotted flap deflected by 15 deg. The flow field that the flap experiences is heavily influenced by the propeller, nacelle, and wing.

It is shown that the flap surface flow field is dominated by the flow from the pressure side of the main element, as well as by the slipstream deformation and the breakdown of the helical vortex system in that region. Spanwise surface friction coefficient distributions show high unsteadiness in C_f at the flap leading edge and both its upper and lower surfaces, originating from the pressure side of the main element. Flow originating from the upper side of the main wing is not seen to cause instability in the flap boundary layer across the span of the wing in present work. Propeller tip vortices do not reach the flap upper surface. The increase in flow momentum by the propeller is clear by the increased friction coefficient within the slipstream and reduces, in general, flow separation on the flap. However, two distinct flow separation regions are observed in current results.

A distinct vortex core beneath the surface of the wing's pressure side originates from the root sections of the propeller blades. The orientation of the vortex introduces a spanwise flow component towards the nacelle centerline. This vortex flow traverses through the cove to the flap suction side. Although the actual vortex breaks apart from the cove onward, the low-energetic vortex flow weakens the flap boundary layer, consequently inducing local flow separation.

A large flow separation zone at the flap exists inboard of the blade-down side slipstream edge. This flow originates from the pressure side of the main wing as well, in this case from the blade-down side of the propeller tips and also transfers through the cove to the upper side of the flap. Streamlines at the flap clearly show an inboard deflection of the

flow near the separated area. This inboard deflection of the streamlines increases the distance traveled along the surface, increasing boundary layer thickness and promoting flow separation. However, the flap flow separation region is complex and not easy to decompose. This paper does not provide a complete insight into the flow behavior, and additional research is necessary to comprehensively analyze the flow and its interaction effects before a definitive conclusion can be reached.

References

[1] Müller, L., Kozulovic, D., and Friedrichs, J., "Unsteady Flow Simulations of an Over-the-wing Propeller Configuration," *50th AIAA/ASME/SAE/ASEE Joint Propulsion Conference*, Cleveland, Ohio, July 2014. https://doi.org/10.2514/6.2014-3886.

[2] Deere, K., Viken, S., Carter, M., Viken, J., Wiese, M., and Farr, N., "Computational Analysis of Powered Lift Augmentation for the LEAPTech Distributed Electric Propulsion Wing," *35th AIAA Applied Aerodynamics Conference*, Denver, Colorado, June 2017. https://doi.org/10.2514/6.2017-3921.

[3] Biser, S., Atanasov, G., Hepperle, M., Filipenko, M., Keller, D., Vechtel, D., Boll, M., Kastner, N., and Noe, M., "Design Space Exploration Study and Optimization of a Distributed Turbo-Electric Propulsion System for a Regional Passenger Aircraft," *AIAA Propulsion and Energy 2020 Forum*, online-only, August 2020. https://doi.org/10.2514/6.2020-3592.

[4] Keller, D., "Towards higher aerodynamic efficiency of propeller-driven aircraft with distributed propulsion," *CEAS Aeronautical Journal*, Vol. 12, No. 4, 2021, pp. 777–791. https://doi.org/10.1007/s13272-021-00535-5.

[5] Duivenvoorden, R. R., Suard, N., Sinnige, T., and Veldhuis, L. L. M., "Experimental Investigation of Aerodynamic Interactions of a Wing with Deployed Fowler Flap under Influence of a Propeller Slipstream," *AIAA AVIATION 2022 Forum*, San Diego, California, July 2022. https://doi.org/10.2514/6.2022-3216.

[6] Roosenboom, E., Heider, A., and Schröder, A., "Propeller Slipstream Development," *25th AIAA Applied Aerodynamics Conference*, Vol. 1, Miami, Florida, June 2007, pp. 1–9.

[7] Roosenboom, E., Heider, A., and Schröder, A., "Comparison of PIV measurements with unsteady RANS calculations in a propeller slipstream," *27th AIAA Applied Aerodynamics Conference*, San Antonio, Texas, June 2009, pp. 1–13. https://doi.org/10.2514/6.2009-3626.

[8] Roosenboom, E. W. M., Stürmer, A., and Schröder, A., "Advanced Experimental and Numerical Validation and Analysis of Propeller Slipstream Flows," *Journal of Aircraft*, Vol. 47, No. 1, 2010, pp. 284–291. https://doi.org/10.2514/1.45961.

[9] Bongen, D., Beckers, M., Schollenberger, M., Bergmann, D. P., Lutz, T., Gothow, A., Saeed, M., Weiss, J., Bardenhagen, A., and Radespiel, R., "Simulation of a Distributed Propulsion System in a Wind Tunnel," *AIAA AVIATION 2022 Forum*, San Diego, California, July 2022. https://doi.org/10.2514/6.2022-3818.

[10] Boermans, L. M. M., and Rutten, P. B., "TU Delft Internal Report LSW 95-3, Two-dimensional aerodynamic characteristics of airfoil NLF-MOD22 with fowler flap," 1995.

[11] Van Arnhem, N., de Vries, R., Sinnige, T., and Veldhuis, L. L. M., *"XPROP-S propeller geometry"*, 2022. https://doi.org/10.5281/zenodo.6355670.

[12] Duivenvoorden, R. R., Sinnnige, T., and Veldhuis, L. L. M., "NOVAIR Distributed Propeller Wing geometry," , 2024. https://doi.org/10.2514/6.2022-3216.

[13] Duivenvoorden, R. R., Sinnnige, T., and Veldhuis, L. L. M., "Experimental dataset of wind tunnel campaigns with a propeller-wing-flap model." , 2024. https://doi.org/10.4121/3161b813-ad38-4f9c-bb9d-333b895f46bc.

[14] Van Arnhem, N., *Unconventional Propeller-Airframe Integration for Transport Aircraft Configurations*, Ph.D. dissertation, Delft University of Technology, The Netherlands, 2022. https://doi.org/10.4233/uuid:4d47b0db-1e6a-4f38-af95-aafd33c29402.

[15] Rumsey, C. L., and Ying, S. X., "Prediction of high lift: review of present CFD capability," *Progress in Aerospace Sciences*, Vol. 38, No. 2, 2002, pp. 145–180. https://doi.org/10.1016/S0376-0421(02)00003-9.

[16] Rumsey, C. L., Slotnick, J. P., Long, M., Stuever, R. A., and Wayman, T. R., "Summary of the First AIAA CFD High-Lift Prediction Workshop," *Journal of Aircraft*, Vol. 48, No. 6, 2011, pp. 2068–2079. https://doi.org/10.2514/1.C031447.

[17] Rumsey, C. L., and Slotnick, J. P., "Overview and Summary of the Second AIAA High Lift Prediction Workshop (Invited)," *Journal of Aircraft*, Vol. 52, No. 4, 2014, pp. 1006–1025. https://doi.org/10.2514/1.C032864.

[18] Rumsey, C. L., and Slotnick, J. P., "Overview and Summary of the Third AIAA High Lift Prediction Workshop," *Journal of Aircraft*, Vol. 56, No. 2, 2019, pp. 621–644. https://doi.org/10.2514/1.C034940.

[19] Götten, F., Finger, D., Marino, M., Bil, C., Havermann, M., and Braun, C., "A review of guidelines and best practices for subsonic aerodynamic simulations using RANS CFD," *Asia-Pacific International Symposium on Aerospace Technology (APISAT)*, Adelaide, December 2019. URL https://search.informit.org/doi/10.3316/informit.938995657936656.

[20] Beckers, M. F., Schollenberger, M., Lutz, T., Bongen, D., Radespiel, R., Florenciano, J. L., and Funes-Sebastian, D. E., "CFD Investigation of High-Lift Propeller Positions for a Distributed Propulsion System," *AIAA AVIATION 2022 Forum*, San Diego, California, July 2022. https://doi.org/10.2514/6.2022-3217.

[21] Suard, N. T., *Improving High Angle of Attack Performance of an Aircraft With Leading Edge Mounted Propellers Through Nacelle and Leading Edge Modification*, MSc. Thesis, Delft University of Technology, The Netherlands, 2022. URL https://repository.tudelft.nl/record/uuid:157c05ac-52b6-4eed-a58e-a5af02c69ea3.

[22] Taniguchi, S., and Oyama, A., "Numerical Analysis of Propeller Mounting Position Effects on Aerodynamic Propeller/Wing Interaction," *AIAA SCITECH 2022 Forum*, San Diego, California, January 2022. https://doi.org/10.2514/6.2022-0153.

[23] Stuermer, A., "Unsteady CFD Simulations of Propeller Installation Effects," *42nd AIAA/ASME/SAE/ASEE Joint Propulsion Conference*, Sacramento, California, July 2006. https://doi.org/10.2514/6.2006-4969.

[24] Stokkermans, T., van Arnhem, N., Sinnige, T., and Veldhuis, L. L. M., "Validation and Comparison of RANS Propeller Modeling Methods for Tip-Mounted Applications," *AIAA Journal*, Vol. 57, No. 2, 2019, pp. 566–580. https://doi.org/10.2514/1.J057398.

[25] Stokkermans, T. C. A., *Aerodynamics of Propellers in Interaction Dominated Flowfields: An Application to Novel Aerospace Vehicles*, Ph.D. dissertation, Delft University of Technology, The Netherlands, 2020. https://doi.org/10.4233/uuid:46178824-bb80-4247-83f1-dc8a9ca7d8e3.

[26] Roosenboom, E., Heider, A., and Schröder, A., "Investigation of the Propeller Slipstream with Particle Image Velocimetry," *Journal of Aircraft*, Vol. 46, No. 2, 2009, pp. 442–449. https://doi.org/10.2514/1.33917.

[27] Zore, K., Parkhi, G., Sasanapuri, B., and Varghese, A., "Ansys Mosai Poly-Hexcore Mesh for High-Lift Aircraft Configuration," *21th Annual CFD Symposium*, Bangalore, India, August 2019.

[28] Ribeiro, A. F., Duivenvoorden, R., and Martins, D., "High-Fidelity Simulations of Propeller-Wing Interactions in High-Lift Conditions," *AIAA AVIATION 2023 Forum*, San Diego, California, June 2023. https://doi.org/10.2514/6.2023-3541.

[29] Qiu, Y., Bai, J., and Qiao, L., "Aerodynamic Effects of Wing-Mounted Engine Nacelle on High-Lift Configuration of Turboprop Airliner," *Journal of Aircraft*, Vol. 55, No. 3, 2017, pp. 1–8. https://doi.org/10.2514/1.C034529.

[30] de Vries, R., van Arnhem, N., Sinnige, T., Vos, R., and Veldhuis, L., "Aerodynamic interaction between propellers of a distributed-propulsion system in forward flight," *Aerospace Science and Technology*, Vol. 118, 2021. https://doi.org/10.1016/j.ast.2021.107009.

[31] Veldhuis, L. L. M., *Propeller Wing Aerodynamic Interference*, Ph.D. dissertation, Delft University of Technology, The Netherlands, 2005. URL http://resolver.tudelft.nl/uuid:8ffbde9c-b483-40de-90e0-97095202fbe3.

[32] Veldhuis, L. L. M., Kotsonis, M., and Berkel, E., "Non-Uniform Inflow Effects on Propeller Performance," *31st AIAA Applied Aerodynamics Conference*, San Diego, California, June 2013. https://doi.org/10.2514/6.2013-2801.

[33] Aultman, M., Wang, Z., Auza-Gutierrez, R., and Duan, L., "Evaluation of CFD methodologies for prediction of flows around simplified and complex automotive models," *Computers Fluids*, Vol. 236, 2022, p. 105297. https://doi.org/https://doi.org/10.1016/j.compfluid.2021.105297.

[34] Felli, M., "Underlying mechanisms of propeller wake interaction with a wing," *Journal of Fluid Mechanics*, Vol. 908, 2021. https://doi.org/10.1017/jfm.2020.792.